RSC Advances

PAPER

View Article Online
View Journal | View Issue

Cite this: *RSC Adv.*, 2022, **12**, 8300

A type II heterojunction α-Fe_2O_3/g-C_3N_4 for the heterogeneous photo-Fenton degradation of phenol†

Fuxiang Ge,[ab] Xuehua Li,[a] Mian Wu,[c] Hui Ding[c] and Xiaobing Li *[a]

The heterogeneous photo-Fenton reaction is an effective method of chemical oxidation to remove phenol in wastewater with environmental friendliness and sustainability. Herein, the composite α-Fe_2O_3/g-C_3N_4, as a catalyst of the heterogeneous photo-Fenton reaction, has been synthesized by hydrothermal-calcination method using the abundant and low-cost $FeCl_3 \cdot 6H_2O$ and g-C_3N_4 as raw materials. The influence of the annealing temperature during calcination was also investigated. The UV-Vis diffuse reflectance spectra of samples show that the composite α-Fe_2O_3/g-C_3N_4 possesses the widest light response range. Furthermore, the transient photocurrent response curves demonstrated the strongest intensity of α-Fe_2O_3/g-C_3N_4. The annealed α-Fe_2O_3/g-C_3N_4 is indicative of the highest degradation efficiency in all samples due to the improvement of the charge transfer ability caused by the tight heterojunction structure. The results of the scavenger trapping experiments show that the hydroxyl radical was the main active species in degradation. Based on experimental results, a type II heterojunction should be built in the composite α-Fe_2O_3/g-C_3N_4, driving the photoelectrons transfer and migration by internal electronic field. This work provides a facile and new method to synthesize α-Fe_2O_3/g-C_3N_4 as an effective heterogeneous photo-Fenton catalyst for environmental remediation.

Received 23rd December 2021
Accepted 18th February 2022

DOI: 10.1039/d1ra09282k

rsc.li/rsc-advances

1 Introduction

Recently, the electronic, automotive and construction industries have driven a rapid growth of bisphenol A, phenolic resin, and raw phenol. However, a large amount of phenol wastewater is inevitably produced in these processes.[1] Phenol has a benzene ring structure with high stability, leading to difficulty in its degradation in a natural environment.[2,3] Phenol can deactivate cellular protein by food chain intake, skin and mucosa. It also can convert into a phenoxy radical in molecular structure due to the loss of electronic behavior, which will result in mutations of DNA or RNA and cancer in chromosome sites.[4] Therefore, how to degrade phenol has received much attention in the field of organic wastewater remediation. Many treatments have been established, including biological, physical and chemical methods. Biological methods face bacteria breeding difficulty and long processing cycles.[5,6] Physical methods require desorption processing and retreatment. Moreover, the removal effect is poor for low concentration conditions. Based on oxidation, the chemical method has attracted increasing attention due to its simple operation, high removal efficiencies, and no secondary pollution.[7,8]

As a typical chemical method, the Fenton reaction forms hydroxyl radicals (˙OH) *via* ferrous ions activating hydrogen peroxide, which can non-selectively remove organic pollutants owing to the high oxidation–reduction potential of +2.80 V.[9] However, the acidic aqueous-based medium (pH = 2.5–4) and huge ferric hydroxide sludge dramatically increase the cost of degradation. The heterogeneous Fenton reaction, using the immobilized solid iron species (≡Fe) instead of the iron ion, not only prevents the generation of sludge, but also widens the pH range of application.[10] Unfortunately, the solid iron has a lower rate of regeneration of ≡Fe(II) than the iron ion. How to accelerate the regeneration of ≡Fe(II) has also become a crucial issue for the heterogeneous Fenton reaction.[11] The heterogeneous photo-Fenton reaction, using a photo-induced electron to accelerate the regeneration of ≡Fe(II), has attracted increasing attention owing to its environmental friendliness and sustainability.[12] Alpha-Fe_2O_3, as a n-type semiconductor, can absorb visible light owing to its inherent band gap of 2.2 eV. It is also a common candidate for the composite photocatalyst of the heterogeneous photo-Fenton reaction as a solid iron source.[13–15] Moreover, it has shown great potential due to its natural abundance, low-cost, high thermal and chemical stability. However, α-Fe_2O_3 suffers from a high recombination rate of

[a]National Engineering Research Center of Coal Preparation and Purification, China University of Mining and Technology, Xuzhou 221000, Jiangsu, China. E-mail: lixh@cumt.edu.cn
[b]Kaifeng Ecological and Environmental Monitoring Center, Henan Province, China
[c]School of Chemical Engineering &Technology, China University of Mining and Technology, Xuzhou, Jiangsu, China

† Electronic supplementary information (ESI) available. See DOI: 10.1039/d1ra09282k

photoinduced electron–hole pairs and narrow visible light response range. Thus, constructing a composite with a suitable band energy gap is a mainstream approach to widen the light absorption region and reduce the charge recombination.[16–20] Graphitic carbon nitride (g-C_3N_4), as a two-dimensional layered semiconductor, has drawn particular attention in photocatalysis due to its element abundance, facile preparation, great visible light activity, high thermal and outstanding chemical stabilities, and excellent electronic structure.[21] Recently, the composite photocatalysts combining α-Fe_2O_3 and g-C_3N_4 have been successfully fabricated and showed great performance in water splitting,[22] carbon dioxide reduction,[23] photochemical reaction,[24] and heavy metal ion reduction.[25]

Although the combination of α-Fe_2O_3 and g-C_3N_4 have been applied in various fields, the use of the composite α-Fe_2O_3/g-C_3N_4 as a heterogeneous photo-Fenton catalyst has been rarely reported to the best of our knowledge. Moreover, there was no composite of α-Fe_2O_3/g-C_3N_4 prepared by hydrothermal-calcination steps to enhance the crystallinity of the nanostructure and further improve the transfer of photo-induced electron–holes. Finally, there is no consensus on whether the composite α-Fe_2O_3/g-C_3N_4 belongs to the Z-scheme or type II heterojunction.[22,26] Based on the above discussions, we introduce a method involving a hydrothermal step first, followed by calcination (hydrothermal-calcination steps), to synthesize a novel photocatalyst for the heterogeneous photo-Fenton degradation of phenol. The calcination step in this combined method aimed to improve the crystallinity, which facilitates the transfer of photo-induced charges. According to characterization measurements, the obtained α-Fe_2O_3/g-C_3N_4 has a wide visible-light responsive feature, tight heterojunction structure, and superior electron transfer ability, which finally lead to the higher degradation of phenol. The photoelectrochemical and scavenger trapping experimental results indicate that a type II heterojunction had been built to drive the photo-induced charge transfer and migration. Under the effect of this internal electronic field, the excited electrons from both components accumulated in the CB of α-Fe_2O_3 and further reduced ≡Fe(III) of the active site to ≡Fe(II), which accelerated the ≡Fe(III)/≡Fe(II) cycles and finally improved the generation of $^{\cdot}OH$ and the degradation efficiency. This work provides a facile new avenue to synthesize the α-Fe_2O_3/g-C_3N_4 composite, and uses it as an effective heterogeneous photo-Fenton catalyst for environmental remediation.

2 Experimental section

2.1 Synthesis

The g-C_3N_4 was prepared by pyrolysis approach. 5 g melamine was heated in a tube furnace from room temperature to 520 °C at a rate of 20 °C min^{-1}. After maintaining the temperature for 2 h, the sample was cooled down to room temperature. Finally, the as-prepared yellow solid was milled into the g-C_3N_4 powder.

The α-Fe_2O_3/g-C_3N_4 sample was fabricated by hydrothermal-calcination steps. In a typical procedure, 0.2 g of g-C_3N_4 and 0.6 g $FeCl_3 \cdot 6H_2O$ were dissolved in 50 mL water, and the solution was heated for 6 h at a temperature of 180 °C in the autoclave. Then, the solid composites were separated from the solution by centrifuging at 3000 rpm for 20 min. After cleaning three times by distilled water, the solid was calcined at 520 °C for 2 h with nitrogen protection to obtain the α-Fe_2O_3/g-C_3N_4 sample.

2.2 Characterization

X-ray diffraction (XRD) was performed on a Panalytical X'Pert PRO system using Cu-Kα radiation. X-ray photoelectron spectroscopy (XPS) analysis was carried out on an X-ray photoelectron spectrometer (PHI 5000 Versa Probe, UIVAC-PHI, Japan). Fourier transform infrared spectroscopy (FTIR) measurements were conducted on a Nicolet 5700 spectrophotometer (Nicolet, USA) in the range of 400–4000 cm^{-1}. Ultraviolet-visible diffuse reflectance spectra (UV-Vis DRS) were measured on a Cary 300 spectrophotometer (Varian, USA). Fluorescence spectra were obtained using a Fluoromax-4 fluorescence spectrophotometer (Horiba, Japan) with different excitation wavelengths.

The transient photocurrent response curves and electrochemical impedance spectroscopy (EIS) curves were measured by electrochemical workstation (Chenhua CHI 760E). The Ag/AgCl electrode and Pt wire were used as the reference electrode and counter electrode, respectively. The working electrode was prepared *via* the following methods. 10 mg of photocatalyst was added to 1 mL of 0.5% Nafion solution, which was subsequently treated by ultrasonication for 10 min. The dispersed solution was dropped onto a fluorine-doped tin oxide glass (with a size of 1 × 1 cm^2) and dried at 50 °C for 4 h in a low vacuum atmosphere. Then, the obtained electrode was inserted in 0.1 mol L^{-1} Na_2SO_4 solution as the electrolyte. Under the irradiation of a 350 W xenon lamp, the photocurrent response curves were measured at a bias potential of 0.1 V and with given irradiation intervals of 30 s. EIS was performed on an applied voltage of 0 V with an amplitude of 5 mV over a frequency range between 10^{-2} and 10^5 Hz.

2.3 Heterogeneous photo-Fenton degradation and radical oxygen species analysis

The heterogeneous photo-Fenton degradation experiments were conducted in an assembled photochemical system, in which a beaker with a volume of 100 mL is placed under a 350 W Xenon lamp with a distance of 10 cm. The lamp surface is 12.5 cm away from the 100 mL scale of the beaker. Before degradation, the lamp was warmed up for 2 min to a rated output intensity of 350 W. Circulating water was introduced to cool the rising temperature in the solution from irradiation.

In a typical degradation procedure, 10 mg α-Fe_2O_3/g-C_3N_4 was added to 100 mL phenol solution with a concentration of 50 mg L^{-1}, and the solution was then stirred for 30 min in the dark to reach adsorption equilibrium. After 45 mM H_2O_2 was added, the solution was irradiated by the xenon lamp. Then, a 3 mL aliquot of the solution was taken out at certain time intervals, and the solid catalysts were separated by centrifugation. Then, the concentration of phenol remaining in solution was determined by UV-Vis spectroscopy at the maximum

absorbance peak of 510 nm. The degradation efficiency formula is defined as:

$$\text{Degradation efficiency } (\%) = \frac{C_0 - C_t}{C_0} \quad (1)$$

where C_0 and C_t represent the concentration of phenol at the initial and desired time intervals, respectively. Control experiments were conducted under the same steps using an equivalent dosage of bare α-Fe_2O_3 and g-C_3N_4 as catalysts. In scavenger trapping experiments, isopropyl alcohol (IPA) and 1,4-benzoquinone (BQ) were added in solution for quenching $^{\bullet}OH$ and $^{\bullet}O_2^-$ radicals, respectively.

3 Results and discussions

3.1 Characterization of the heterogeneous photocatalyst

The crystal structures of g-C_3N_4, α-Fe_2O_3 and α-Fe_2O_3/g-C_3N_4 were investigated by XRD technique and the results are shown in Fig. 1(a). The g-C_3N_4 sample shows a characteristic diffraction peak at 13.2°, which is indexed to the (100) diffraction plane and corresponds to the in-plane tri-*s*-thiazine repeating motifs. Another prominent peak is located at 27.5°, which is assigned to the (002) plane of the interlayer stacking of the conjugated aromatic systems.[27] The characteristic diffraction peaks of iron oxide are present at $2\theta = 24.3°$, 33.3°, 35.9°, 41.0°, 49.6°, 54.3°, 62.6° and 64.1°, which correspond to the (012), (104), (110), (113), (024), (116), (214) and (300) diffraction planes of α-Fe_2O_3,[28] indicating that the iron oxide is hematite. The composite α-Fe_2O_3/g-C_3N_4 shows all of the characteristic diffraction peaks of g-C_3N_4 and α-Fe_2O_3, suggesting the success of the combination.

The specific surface area and porosity are of great importance for the absorption of contaminants and transmission of radical oxygen species, respectively. The nitrogen adsorption–desorption isotherm and the pore size distribution curve of α-Fe_2O_3/g-C_3N_4 were obtained and are shown in Fig. 1(b), including the BET surface area, total pore volume and average pore size. The isotherm showed that α-Fe_2O_3/g-C_3N_4 presents a typical IV pattern in the range of 0.5–0.98 relative pressure, indicating the presence of a mesoporous structure in the size of 2–50 nm. According to the IUPAC classification, the hysteresis loop of the isotherm was type H3,[24] which indicates that narrow slit-shaped pores are associated with the structure of the plate-like g-C_3N_4 and α-Fe_2O_3 nanoparticles. The surface area and average pore diameter of α-Fe_2O_3/g-C_3N_4 were calculated to be 28.75 $m^2\ g^{-1}$ and 10.2 nm, respectively.

The ability to harvest visible light plays an important role in improving the photocatalytic activity (degradation in current work) for photocatalysts because visible light accounts for nearly half of the solar spectrum. The UV-Vis diffuse reflectance spectra of g-C_3N_4, α-Fe_2O_3 and α-Fe_2O_3/g-C_3N_4 were measured and are shown in Fig. 2. For pure g-C_3N_4, the characteristic spectrum shows a fundamental absorption edge at 470 nm, corresponding to a band gap energy of 2.7 eV, which is in great agreement with the previous reports.[27] The as-prepared α-Fe_2O_3 has an absorption edge at approximately 630 nm ascribed to the intrinsic band gap. Both components have the ability to absorb visible light. Compared with α-Fe_2O_3 or g-C_3N_4, α-Fe_2O_3/g-C_3N_4 showed a significant increase in visible light absorption due to the synergy of both materials.

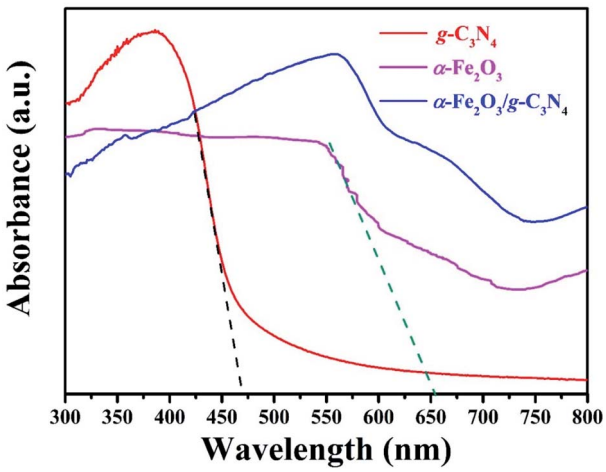

Fig. 2 UV-Vis diffuse reflectance spectra of g-C_3N_4, α-Fe_2O_3 and α-Fe_2O_3/g-C_3N_4.

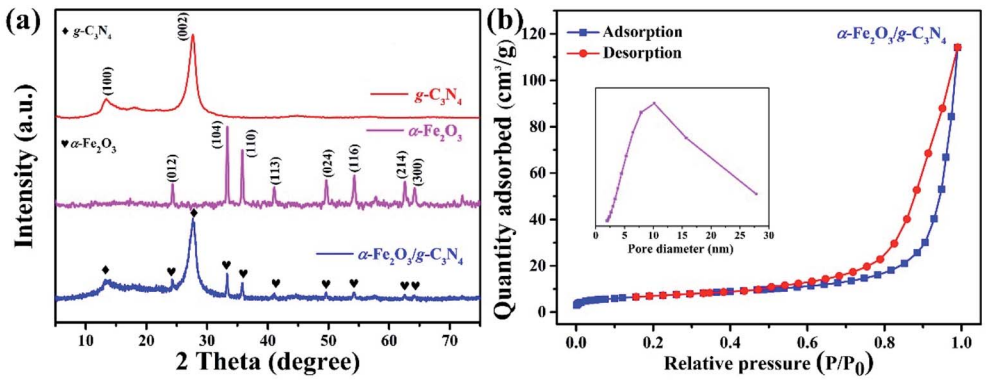

Fig. 1 (a) XRD patterns of g-C_3N_4, α-Fe_2O_3 and α-Fe_2O_3/g-C_3N_4. (b) Nitrogen sorption isotherms and corresponding pore size distributions (inset) of α-Fe_2O_3/g-C_3N_4. (c) UV-Vis diffuse reflectance spectra of g-C_3N_4, α-Fe_2O_3 and α-Fe_2O_3/g-C_3N_4.

XPS has been carried out to deeply evaluate the binding energy of the elements and surface groups in the composite catalyst. As shown in Fig. 3(a), the survey spectra of α-Fe_2O_3/g-C_3N_4 show several characteristic peaks at around 284.8, 399.0, 532.0 and 723 eV, corresponding to C 1s, N 1s, O 1s and Fe 2p, respectively, and indicate the existence of these elements. The high-resolution C 1s spectrum of α-Fe_2O_3/g-C_3N_4 shows three peaks located at 284.6, 286.3 eV and 288.1 eV, which are assigned to the C–C bonding of the sp^2-hybridized carbon, C–N bonding groups and sp^2-hybridized bonding of the N–C=N bonds, respectively (Fig. 3(b)).[29,30] The N 1s spectrum of α-Fe_2O_3/g-C_3N_4 also could be deconvoluted into three characteristic peaks at around 398.1, 399.2 and 400.1 eV, which were attributed to pyridinic nitrogen (C–N=C), pyrrolic nitrogen (C–N–C) and quaternary nitrogen (N–$(C)_3$), respectively (Fig. 3(c)).[31,32] The O 1s peak has three deconvolution peaks at 531.9, 532.8 and 530.7 eV in Fig. 3(d), corresponding to the bonds of C–O, C=O and Fe–O–C, respectively. The existence of Fe–C–O indicated the strong interaction between the α-Fe_2O_3 moiety and g-C_3N_4 moiety, which might serve as an electron pathway to facilitate

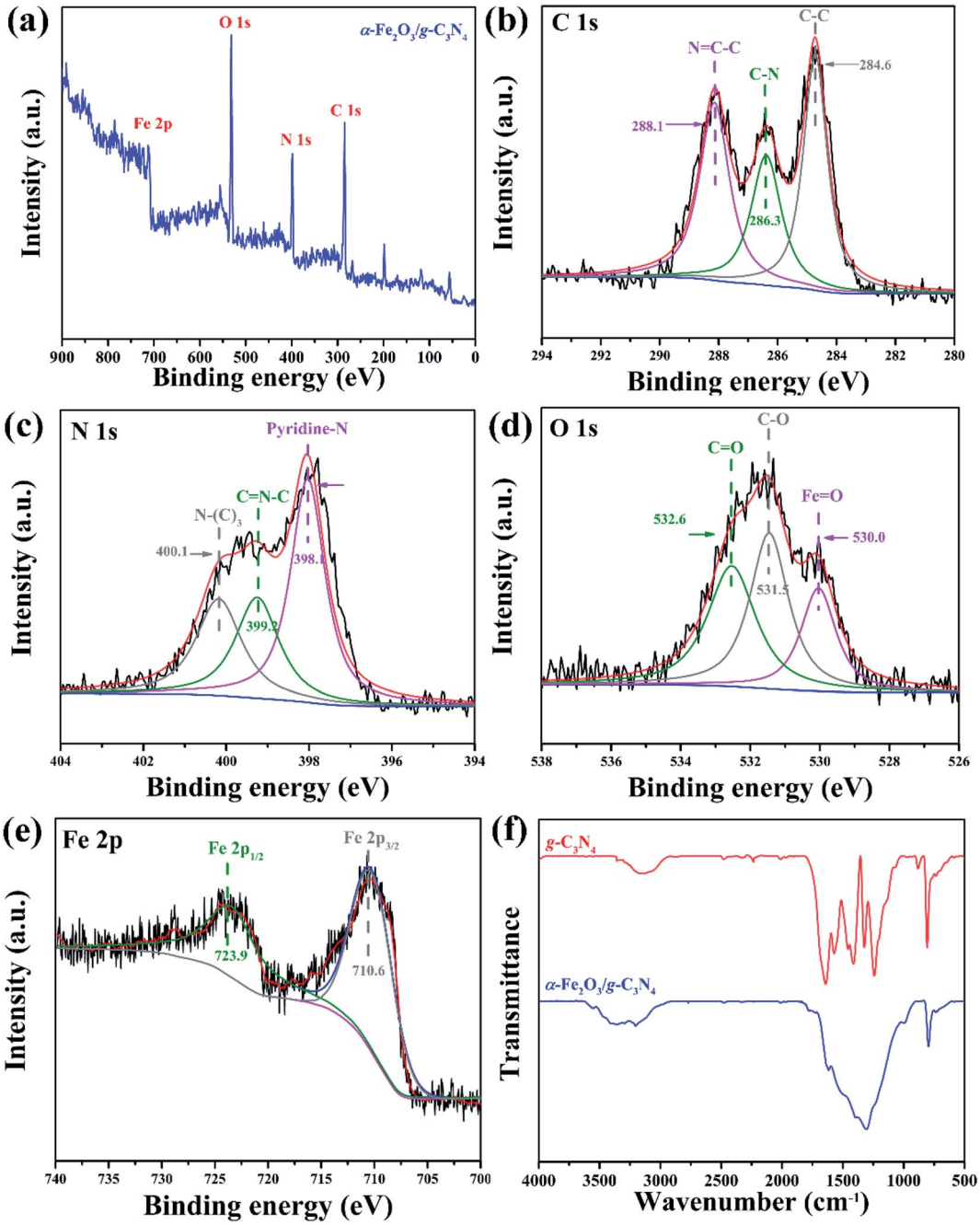

Fig. 3 (a) XPS survey spectrum of α-Fe_2O_3/g-C_3N_4. The high-resolution binding energy spectra of (b) C 1s, (c) N 1s, (d) O 1s, and (e) Fe 2p. The (f) FTIR spectra of g-C_3N_4, and α-Fe_2O_3/g-C_3N_4.

electron transfer and migration between interfaces.[33] In the high-resolution spectra of Fe 2p (Fig. 3(e)), the composite has two obvious peaks at 710.6 and 724.5 eV, corresponding to Fe $2p_{3/2}$ and Fe $2p_{1/2}$, respectively. In addition, both peaks are fully consistent with the typical values of Fe in α-Fe_2O_3,[34] suggesting the formation of α-Fe_2O_3.

FTIR spectra were measured to verify the functional groups of g-C_3N_4 and α-Fe_2O_3/g-C_3N_4, which are shown in Fig. 3(f). For pure g-C_3N_4, the sharp peak at 806 cm^{-1} originates from the breathing mode of the triazine unit. The α-Fe_2O_3/g-C_3N_4 composite shows the same peak at 806 cm^{-1} with lower intensity, indicating that the triazine unit is still the main structure after the formation of the composite. Several peaks at 1242, 1323, 1407 and 1454 cm^{-1} in the range of 1200–1500 cm^{-1} are ascribed to the typical stretching modes of the C–N heterocycles of g-C_3N_4, and the peak at 1647 cm^{-1} corresponds to the C=N stretching vibration.[35] These peaks merged into a broad peak in the α-Fe_2O_3/g-C_3N_4 composite due to the covering influence of α-Fe_2O_3 on the surface of g-C_3N_4. Both g-C_3N_4 and α-Fe_2O_3/g-C_3N_4 have a broad peak located in the range of 3300–2900 cm^{-1}, which is assigned to the N–H stretching vibration. These results illustrate that both composites maintain the same polycondensation structure as pure g-C_3N_4.

3.2 Degradation tests

The performance of the as-prepared α-Fe_2O_3/g-C_3N_4 was evaluated by testing the degradation efficiency of phenol (concentration 100 mg L^{-1}). First, the influence of the components in the composite on degradation efficiency was investigated, and the results are shown in Fig. 4(a). As a semiconductor and solid iron source, α-Fe_2O_3 not only can absorb visible light, but also can decompose H_2O_2 into $^{\cdot}OH$ radicals by transferring an electron to H_2O_2 through its active site. The bare α-Fe_2O_3 shows a poor degradation efficiency of about 55% in 70 min. Although α-Fe_2O_3 was able to degrade phenol, the removal efficiency was limited by the low light absorption ability and high electron–hole recombination. The strategy of combining with other semiconductors is a mainstream method to alleviate these limitations. After combining with g-C_3N_4, the composite α-Fe_2O_3/g-C_3N_4 showed a significant improvement in the degradation efficiency up to 90% under the same conditions. The introduction of g-C_3N_4 improves the absorption ability in the visible range (as shown in Fig. 2), and was developed to achieve the spatial separation of the electron and holes between different components and prevent the charge recombination through electron–hole trapping.

The results of phenol degradation by photocatalysts, heterogeneous Fenton reaction and heterogeneous photo-Fenton reaction are shown in Fig. 4 (b). The phenol was not degraded by H_2O_2 in the dark, suggesting that H_2O_2 does not decompose into $^{\cdot}OH$ without the catalyst and light irradiation. When only adding catalysts in the same condition of darkness (heterogeneous Fenton reaction), the degradation efficiency of phenol increased up to 33%, indicating that α-Fe_2O_3/g-C_3N_4 catalytically decomposed H_2O_2 into $^{\cdot}OH$ as the iron source. After irradiation by a xenon lamp for 70 min, about 30% phenol in the solution was degraded in the presence of H_2O_2 and without a catalyst (photo-Fenton reaction), which was attributed to the decomposition of H_2O_2 into $^{\cdot}OH$ by an ultraviolet ray of simulated light.[35] Although both methods slightly increased the degradation efficiency of phenol, the degradation efficiency was still moderate. Under heterogeneous photo-Fenton conditions (heterogeneous photocatalysts, H_2O_2 and light irradiation), the degradation efficiency of phenol was significantly boosted up to 90%. It is worth noting that the total degradation efficiency is not a simple superposition of the efficiency of each part. This result is indicative of a synergistic effect between the heterogeneous Fenton reaction and photo-Fenton reaction, which will be further investigated in the mechanism analysis section.

The degradation performance of α-Fe_2O_3/g-C_3N_4 without the annealing step and under a different annealing temperature was also investigated to provide better insights, which is shown in Fig. S1 (ESI†). It was found that the degradation efficiency of α-Fe_2O_3/g-C_3N_4 showed a significant increase after calcination, indicating that calcination has a promoting effect on the degradation process due to the improvement of the photo-induced charge transfer. Moreover, as the annealing temperatures increase from 360 °C to 520 °C, the degradation only slightly increased about 24%. Nevertheless, when the annealing temperature was up to 560 °C, the obtained efficiency decreased

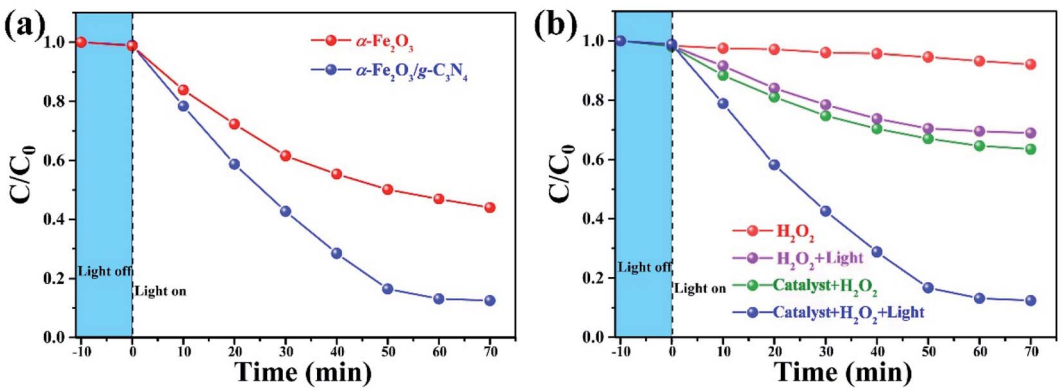

Fig. 4 Phenol degradation profile under different conditions (a) and with different photocatalysts (b).

from 92 to 60%, which be attributed to the decomposition of some g-C_3N_4 caused by excessive temperature.

A series of experiments were carried out to obtain the optimal degradation conditions, including photocatalyst amounts, H_2O_2 dosage, pH value and initial contaminant concentration, as shown in Fig. 5. It is generally known that adding some quantity of catalysts directly affects the H_2O_2 decomposition. Fig. 5(a) compares the degradation performance when various catalyst concentrations were added to the solutions. The degradation efficiencies of phenol increased with increasing catalyst concentration from 0.05 to 0.15 mg L^{-1}. This is because of the boost of $^{\bullet}OH$ from the decomposition of H_2O_2 catalyzed by α-Fe_2O_3/g-C_3N_4. However, when the concentration increased from 0.15 to 0.25 mg L^{-1}, the degradation efficiency slightly decreased. This is attributed to the excessive iron species consuming some $^{\bullet}OH$ radicals. The influence of the H_2O_2 dosage shown in Fig. 5(b). It could be easily found that the degradation efficiencies remained at the high level of about 90% in 70 min, when the dosage increased from 90 to 180 mmol L^{-1}. The efficiencies would decrease when the dosage was below or above this range. This was because of the lockage of H_2O_2 leading to less $^{\bullet}OH$ radicals or the scavenging effect of excessive H_2O_2 reducing the availability of $^{\bullet}OH$, respectively. At different pH values of 2.5–7.5, as shown in Fig. 5(c), the degradation efficiencies gradually decreased with increasing pH values. However, the α-Fe_2O_3/g-C_3N_4 catalyst shows good performance in the range of 2.5–5.5, wherein at least 81% phenol was degraded in 70 min. The decrease of efficiency in an alkaline environment is associated with the self-decompositions of H_2O_2 molecules and weak oxidation potential of $^{\bullet}OH$ radicals at higher pH (E_0 = +2.8 V and +2.0 V at pH = 0 and 14, respectively).[34] The initial concentration of phenol is another important factor that affects the degradation, as shown in Fig. 5(d). The degradation performance decreased with increasing contaminant concentration. When the initial concentration increased from 50 mg L^{-1} to 100 mg L^{-1}, the degradation efficiency was maintained at 90% in 70 min. Subsequently, the efficiency decreased with an increase of the phenol concentration, which can be attributed to the limitation of reaction sites on the surface of the photocatalyst.

The reusability of composite α-Fe_2O_3/g-C_3N_4 is a crucial factor for its practical and industrial applications. To explore this performance, recycling experiments were carried out. As illustrated in Fig. S2 (ESI†), there was a slight decrease of about 8% in the degradation efficiencies after five cycles, indicating that the composite retained good reusability after undergoing five reaction cycles. The slight decrease in the catalytic performance is unavoidable, which is because of the difficulty in the full recovery of the spent catalyst and pore blockage on the

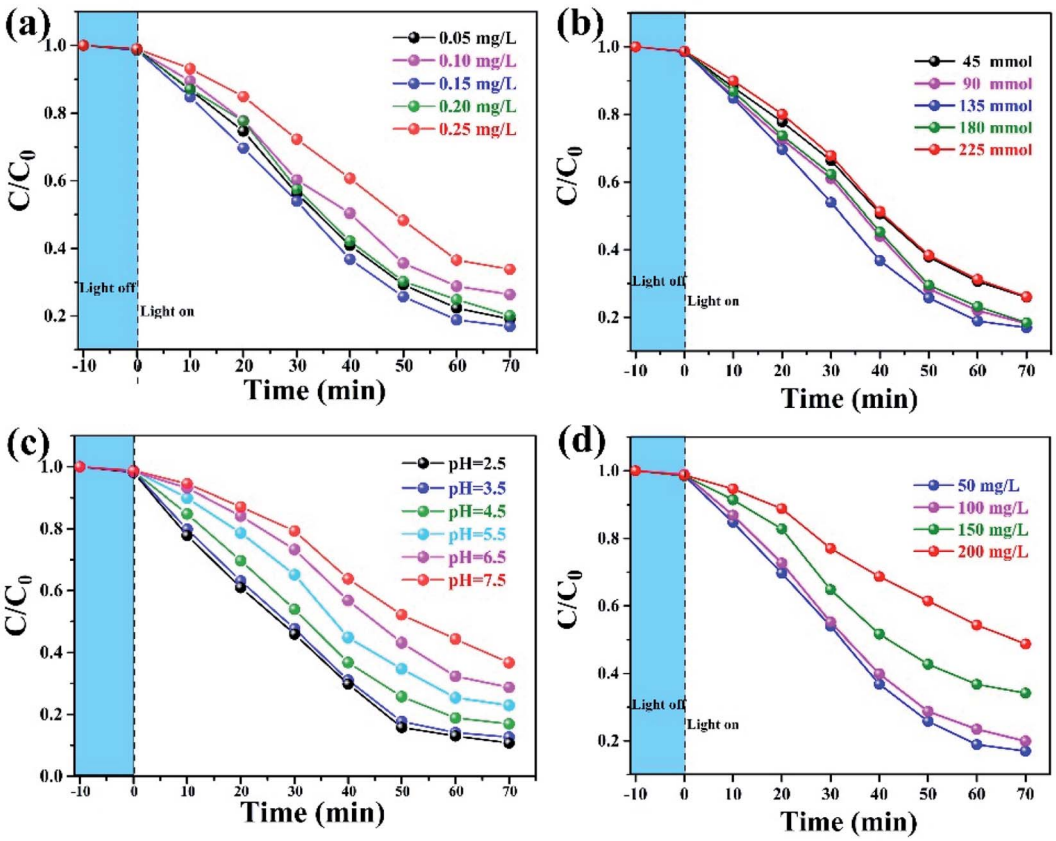

Fig. 5 Effects of the removal experimental conditions on the degradation efficiency, (a) photocatalyst amount, (b) H_2O_2 dosage, (c) pH value, and (d) initial contaminant concentration.

catalyst surface caused by pollutants and residual intermediates.

3.3 Possible mechanism of the heterogeneous photo-Fenton reaction

The photoelectrochemical technique was used to investigate the separation and transfer behaviors of the photo-induced electron–hole pairs in the α-Fe_2O_3/g-C_3N_4 catalyst, including the transient photocurrent response and electrochemical impedance spectroscopy (EIS). As shown in the transient photocurrent response curves of Fig. 6(a), g-C_3N_4 and α-Fe_2O_3/g-C_3N_4 have stable photocurrent cycles under on-off light irradiation cycles. The α-Fe_2O_3/g-C_3N_4 composite shows a photocurrent density of 5.68 μA cm^{-2}, which is about 5 times than that of g-C_3N_4. The well-engineered bandgap arrangement of α-Fe_2O_3/g-C_3N_4 is responsible for the higher performance by facilitating both charge separation and transfer through an internal electric field. During the formation of α-Fe_2O_3 on the surface of g-C_3N_4, some key chemical bonds like Fe–O–C were formed at the same time, and were also revealed by the XPS and FTIR results. These bonds act as a bridge or channel-linked g-C_3N_4 with α-Fe_2O_3, enhancing the interfacial contact of adjacent semiconductors and accelerating the transfer or migration of photo-induced charges between different semiconductors.[35] These improvements were further demonstrated by the EIS spectra of g-C_3N_4 and α-Fe_2O_3/g-C_3N_4 in Fig. 6(b). The α-Fe_2O_3/g-C_3N_4 composite shows a much smaller arc radius than pure g-C_3N_4, indicating the lowest charge transfer resistance during the photo-excited process. The formed chemical bonds between the semiconductors could reduce the transfer resistance of the photo-induced charges. The photoelectrochemical results showed that α-Fe_2O_3/g-C_3N_4 has more separation efficiency and faster interfacial charge transfer behaviors than g-C_3N_4.

In addition, the type of active species in degradation is crucial to elucidate the mechanism of the heterogeneous photo-Fenton reaction. Thus, a series of quenchers (IPA and BQ) were used to scavenge possible species in degradation, such as the hydroxyl radical (˙OH) and superoxide radical (˙O_2^-), and the results are shown in Fig. 7(a). A significant inhibition phenomenon is observed after the ˙OH scavenger (IPA) is added to the reaction system. The degradation efficiency decreased from 90% to 12% in 70 min. In contrast, a slight inhibition of BQ as a scavenger for the superoxide radical was detected from 90 to 86%. These results indicate that the hydroxyl radical, rather than the superoxide radical, is the main active species in this degradation.

Based on the above trapping experiments, a photo-induced charge transfer and generation of ˙OH was proposed for α-Fe_2O_3/g-C_3N_4 as the heterogeneous photo-Fenton catalyst, which is shown in Fig. 7(b). Both g-C_3N_4 and α-Fe_2O_3 generated electrons and holes under visible irradiation due to the intrinsic energy band structure, in which an electron jumps up to the conduction band (CB) and a hole is left in the valence band (VB). Many previous reports demonstrate that the CB and VB of g-C_3N_4 are located at −1.10 eV and +1.6 eV (*vs.* NHE),[36,37] while the CB and VB of α-Fe_2O_3 are located at +0.3 eV and +2.4 eV (*vs.* NHE),[38,39] respectively. According to these energy level structures, two potential alignments of the band energy were proposed for the mechanism of the electron–hole pair transfer and migration in the α-Fe_2O_3/g-C_3N_4 composite, including the type II or Z-scheme heterojunction. If a Z-scheme alignment would be built, the electron in CB of α-Fe_2O_3 will transfer to and further recombine with the holes in VB of g-C_3N_4. This would lead to an enhanced driving force for charge transfer because of the lower CB position of g-C_3N_4 and higher VB location of α-Fe_2O_3. However, the electron accumulated in CB of g-C_3N_4 will transfer to O_2 molecules, and inevitably generate a lot of ˙O_2^- species in the degradation reaction. This is due to it being more negative CB than the redox potential of O_2/˙O_2^- (−0.33 eV). This hypothesis contradicts the results of the scavenger trapping experiment, in which only a few ˙O_2^- species were detected in the reaction.

Hence, a mechanism based on a type II heterojunction should be reasonable. As shown in Fig. 7(b), the excited holes in the VB of α-Fe_2O_3 transfer to the VB of g-C_3N_4, while the electrons in the CB of g-C_3N_4 will transfer to and accumulate in the CB of α-Fe_2O_3. Compared to the dissolved oxygen molecule in solution with a potential barrier at the solid–liquid interface,

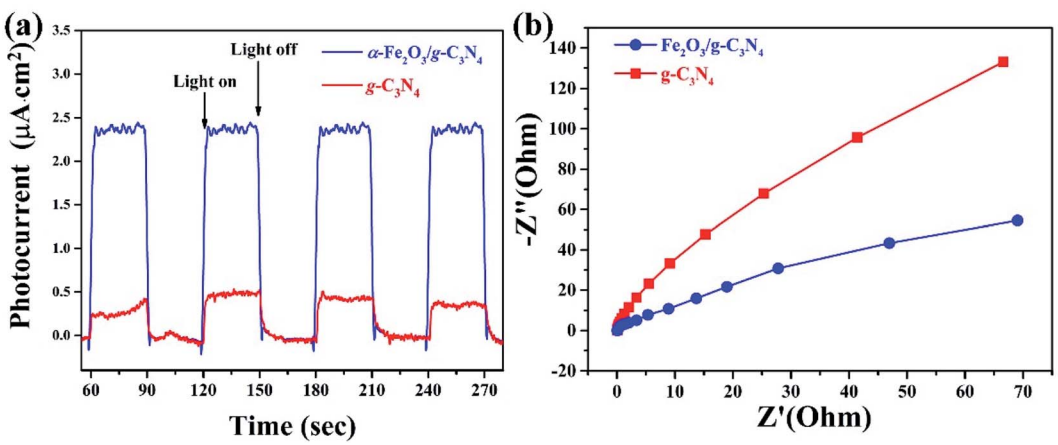

Fig. 6 (a) Transient photocurrents and (b) EIS spectra of g-C_3N_4 and α-Fe_2O_3/g-C_3N_4.

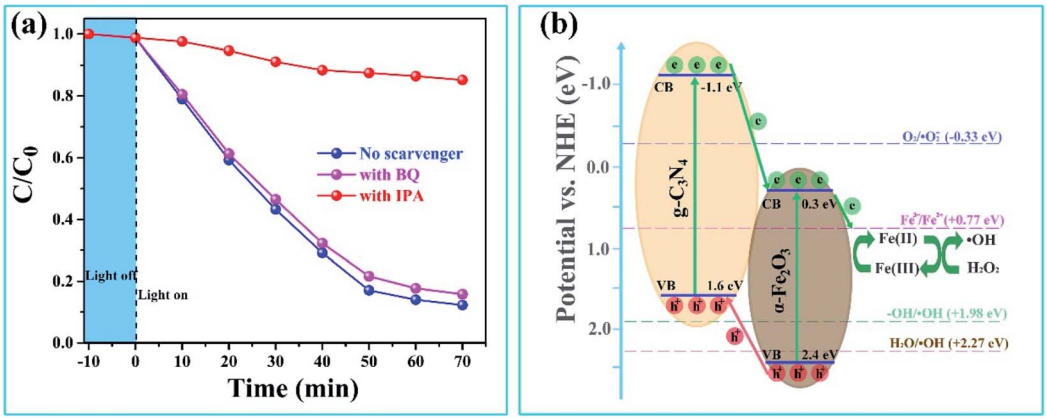

Fig. 7 (a) Degradation of phenol over α-Fe_2O_3/g-C_3N_4 with the addition of different radical scavengers. (b) The proposed heterogeneous photo-Fenton mechanism of α-Fe_2O_3/g-C_3N_4.

the photo-induced electron in the CB of α-Fe_2O_3 was more inclined to transfer to the CB of g-C_3N_4 due to the tight solid–solid interface. The semiconductor of α-Fe_2O_3 not only generated electrons under irradiation, but also obtained the photoelectron from the CB of g-C_3N_4. The accumulated electrons reduced ≡Fe(III) of the iron site to ≡Fe(II) in α-Fe_2O_3. This is because the CB of α-Fe_2O_3 (+0.30 eV) is more negative than the standard potential of Fe^{3+}/Fe^{2+} (+0.77 eV).[37] Hence, these photo-induced electrons from the excitation of α-Fe_2O_3 and g-C_3N_4 accelerated the ≡Fe(III)/≡Fe(II) recycling in the component of α-Fe_2O_3. The obtained ≡Fe(II) would further decompose H_2O_2 into ˙OH, as discussed in many previous heterogeneous photo-Fenton reports, wherein ˙OH takes a dominant role in the degradation of organic contaminants. In addition, due to the redox potential of –OH/˙OH (+1.98 eV) and H_2O/˙OH (+2.27 eV) being more positive than the VB value of g-C_3N_4 (+1.60 eV), the photo-induced holes accumulated on the VB of g-C_3N_4 were not sufficiently positive to form the ˙OH radical.[40,41] This indicated that the ˙OH radicals in the degradation were mainly produced by a heterogeneous photo-Fenton reaction.

4 Conclusions

Heterogeneous photo-Fenton degradation offers a green and sustainable approach to remove phenol in wastewater by using solar energy. As typical semiconductors for photocatalysis, α-Fe_2O_3 and g-C_3N_4 have shown great potential due to their natural abundance, low-cost, high thermal and chemical stability. Herein, a heterogeneous catalyst of α-Fe_2O_3/g-C_3N_4 for the photo-Fenton reaction was synthesized by hydrothermal-calcination method. The results from the UV-Vis DRS and transient photocurrent response curves demonstrated that the α-Fe_2O_3/g-C_3N_4 composite possesses the optimal performance in photocatalysis. The calcination process played an important role in improving the transfer of photo-induced charges by tightening the heterojunction structure. Both improvement of light absorption and photoelectron transfer led to the best degradation efficiency of α-Fe_2O_3/g-C_3N_4. To better understand the mechanism of action, scavenger trapping experiments were carried out to measure the active species in degradation. The results show that the hydroxyl radical was the main active species. Based on these experimental results, a type II heterojunction should be built in the α-Fe_2O_3/g-C_3N_4 composite driving the photoelectrons transfer and migration by internal electronic field. Additionally, a reusability study of α-Fe_2O_3/g-C_3N_4 showed only a slight decrease of the degradation efficiency (about 8%) after five cycles. Overall, α-Fe_2O_3/g-C_3N_4 proved to be an effective heterogeneous photo-Fenton catalyst for environmental remediation.

Conflicts of interest

All authors declare that there are no competing interests.

Acknowledgements

This work is financially supported by the National Natural Science Foundation of China (No. 52004279), Jiangsu Province Key Research and Development Project (BE2018635) and Six Talents Peaks Project in Jiangsu Province (JNHB-077).

References

1 E. Brillas and S. Garcia-Segura, Benchmarking recent advances and innovative technology approaches of Fenton, photo-Fenton, electro-Fenton, and related processes: A review on the relevance of phenol as model molecule, *Sep. Purif. Technol.*, 2020, **237**, 116337.
2 L. Yu, J. Chen, Z. Liang, W. Xu, L. Chen and D. Ye, Degradation of phenol using Fe_3O_4-GO nanocomposite as a heterogeneous photo-Fenton catalyst, *Sep. Purif. Technol.*, 2016, **171**, 80–87.
3 T. W. Leal, L. A. Lourenco, H. d. L. Brandao, A. da Silva, S. M. A. G. U. de Souza and A. A. U. de Souza, Low-cost iron-doped catalyst for phenol degradation by heterogeneous Fenton, *J. Hazard. Mater.*, 2018, **359**, 96–103.

4 A. M. Salazar-Arias, G. I. Giraldo-Gomez and N. R. Sanabria-Gonzalez, Degradation of phenol using mill scale as a Fenton-type catalyst, *Water Environ. J.*, 2019, **34**, 183–191.

5 C. Justino, A. G. Marques, K. R. Duarte, A. C. Duarte, R. Pereira, T. Rocha-Santos and A. C. Freitas, Degradation of phenols in olive oil mill wastewater by biological, enzymatic, and photo-Fenton oxidation, *Environ. Sci. Pollut. Res.*, 2010, **17**(3), 650–656.

6 M. Tyagi, N. Kumari and S. Jagadevan, A holistic Fenton oxidation-biodegradation system for treatment of phenol from coke oven wastewater: Optimization, toxicity analysis and phylogenetic analysis, *J. Water Process. Eng.*, 2020, **37**, 101475.

7 Y. Yavuz, A. S. Koparal and U. B. Ogutveren, Phenol removal through chemical oxidation using Fenton reagent, *Chem. Eng. Technol.*, 2007, **30**(5), 583–586.

8 N. Inchaurrondo, C. P. Ramos, G. Zerjav, J. Font, A. Pintar and P. Haure, Modified diatomites for Fenton-like oxidation of phenol, *Microporous Mesoporous Mater.*, 2017, **239**, 396–408.

9 L. Clarizia, D. Russo, I. Di Somma, R. Marotta and R. Andreozzi, Homogeneous photo-Fenton processes at near neutral pH: A review, *Appl. Catal., B*, 2017, **209**, 358–371.

10 P. V. Nidheesh, Heterogeneous Fenton catalysts for the abatement of organic pollutants from aqueous solution: a review, *RSC Adv.*, 2015, **5**(51), 40552–40577.

11 L. Lyu and C. Hu, Heterogeneous Fenton Catalytic Water Treatment Technology and Mechanism, *Prog. Chem.*, 2017, **29**(9), 981–999.

12 A. N. Soon and B. H. Hameed, Heterogeneous catalytic treatment of synthetic dyes in aqueous media using Fenton and photo-assisted Fenton process, *Desalination*, 2011, **269**, 1–16.

13 J. Liu, B. Wang, Z. Li, Z. Wu, K. Zhu, J. Zhuang, Q. Xi, Y. Hou, J. Chen, M. Cong, J. Li, G. Qian and Z. Lin, Photo-Fenton reaction and H_2O_2 enhanced photocatalytic activity of alpha-Fe_2O_3 nanoparticles obtained by a simple decomposition route, *J. Alloys Compd.*, 2019, **771**, 398–405.

14 L. Guo, F. Chen, X. Fan, W. Cai and J. Zhang, S-doped alpha-Fe_2O_3 as a highly active heterogeneous Fenton-like catalyst towards the degradation of acid orange 7 and phenol, *Appl. Catal., B*, 2010, **96**, 162–168.

15 Y. Liu, W. Jin, Y. Zhao, G. Zhang and W. Zhang, Enhanced catalytic degradation of methylene blue by alpha-Fe_2O_3/graphene oxide *via* heterogeneous photo-Fenton reactions, *Appl. Catal., B*, 2017, **206**, 642–652.

16 M. K. Ahmed, A. E. Shalan, M. Afifi, M. M. El-Desoky and S. Lanceros-Méndez, Silver-Doped Cadmium Selenide/Graphene Oxide-Filled Cellulose Acetate Nanocomposites for Photocatalytic Degradation of Malachite Green toward Wastewater Treatment, *ACS Omega*, 2021, **6**(36), 23129–23138.

17 S. A. Mousa, A. E. Shalan, H. H. Hassan, A. A. Ebnawaled and S. A. Khairy, Enhanced the photocatalytic degradation of titanium dioxide nanoparticles synthesized by different plant extracts for wastewater treatment, *J. Mol. Struct.*, 2022, **1250**, 131912.

18 M. Batool, M. F. Nazar, A. Awan, M. B. Tahir, A. Rahdar, A. E. Shalan, S. Lanceros-Méndez and M. N. Zafar, Bismuth-based heterojunction nanocomposites for photocatalysis and heavy metal detection applications, *Nano-Struct. Nano-Objects*, 2021, **27**, 100762.

19 A. E. Shalan, M. Afifi, M. M. El-Desoky and M. K. Ahmed, Electrospun nanofibrous membranes of cellulose acetate containing hydroxyapatite co-doped with Ag/Fe: morphological features, antibacterial activity and degradation of methylene blue in aqueous solution, *New J. Chem.*, 2021, **45**(20), 9212–9220.

20 M. F. Sanad, A. E. Shalan, M. A. Ahmed and M. F. A. Messih, The controlled synthesis and DFT investigation of novel (0D)–(3D) ZnS/SiO_2 heterostructures for photocatalytic applications, *RSC Adv.*, 2021, **11**(36), 22352–22364, DOI: 10.1039/D1RA02284A.

21 J. Q. Wen, J. Xie, X. B. Chen and X. Li, A review on g-C_3N_4-based photocatalysts, *Appl. Surf. Sci.*, 2017, **391**, 72–123.

22 X. She, J. Wu, H. Xu, J. Zhong, Y. Wang, Y. Song, K. Nie, Y. Liu, Y. Yang, M.-T. F. Rodrigues, R. Vajtai, J. Lou, D. Du, H. Li and P. M. Ajayan, High Efficiency Photocatalytic Water Splitting Using 2D alpha-Fe_2O_3/g-C_3N_4 Z-Scheme Catalysts, *Adv. Energy Mater.*, 2017, **7**(17), 1700025.

23 Z. Jiang, W. Wan, H. Li, S. Yuan, H. Zhao and P. K. Wong, A Hierarchical Z-Scheme alpha-Fe_2O_3/g-C_3N_4 Hybrid for Enhanced Photocatalytic CO_2 Reduction, *Adv. Mater.*, 2018, **30**(10), 1706108.

24 S. Liu, S. Wang, Y. Jiang, Z. Zhao, G. Jiang and Z. Sun, Synthesis of Fe_2O_3 loaded porous g-C_3N_4 photocatalyst for photocatalytic reduction of dinitrogen to ammonia, *Chem. Eng. J.*, 2019, **373**, 572–579.

25 S. Balu, Y.-L. Chen, R. C. Juang, T. C. K. Yang and J. C. Juan, Morphology-Controlled Synthesis of alpha-Fe_2O_3 Nanocrystals Impregnated on g-C_3N_4-SO_3H with Ultrafast Charge Separation for Photoreduction of Cr (VI) Under Visible Light, *Environ. Pollut.*, 2020, **267**, 115491.

26 L. Kong, J. Yan, P. Li and S. F. Liu, Fe_2O_3/C-C_3N_4-Based Tight Heterojunction for Boosting Visible Light-Driven Photocatalytic Water Oxidation, *ACS Sustainable Chem. Eng.*, 2018, **6**(8), 10436–10444.

27 S. W. Cao, J. X. Low, J. G. Yu and M. Jaroniec, Polymeric Photocatalysts Based on Graphitic Carbon Nitride, *Adv. Mater.*, 2015, **27**(13), 2150–2176.

28 Q. Liu, T. Chen, Y. Guo, Z. Zhang and X. Fang, Grafting Fe(III) species on carbon nanodots/Fe-doped g-C_3N_4 *via* interfacial charge transfer effect for highly improved photocatalytic performance, *Appl. Catal., B*, 2017, **205**, 173–181.

29 Y. Deng, L. Tang, C. Feng, G. Zeng, J. Wang, Y. Lu, Y. Liu, J. Yu, S. Chen and Y. Zhou, Construction of Plasmonic Ag and Nitrogen-Doped Graphene Quantum Dots Codecorated Ultrathin Graphitic Carbon Nitride Nanosheet Composites with Enhanced Photocatalytic Activity: Full-Spectrum Response Ability and Mechanism Insight, *ACS Appl. Mater. Interfaces*, 2017, **9**(49), 42816–42828.

30 J. Ju and W. Chen, Synthesis of highly fluorescent nitrogen-doped graphene quantum dots for sensitive, label-free detection of Fe (III) in aqueous media, *Biosens. Bioelectron.*, 2014, **58**, 219–225.

31 S. S. Yi, J. M. Yan and Q. Jiang, Carbon quantum dot sensitized integrated Fe_2O_3@g-C_3N_4 core-shell nanoarray photoanode towards highly efficient water oxidation, *J. Mater. Chem. A*, 2018, **6**(21), 9839–9845.

32 X. Shi, X. Li, G. Liu, M. Du, J. Zhang, G. Liu and Q. Lu, NaCl-assisted synthesis of Fe^{2+} self-doped Fe_2O_3/C_3N_4 nanosheets as efficient Fenton catalyst, *J. Mater. Sci.*, 2020, **55**(23), 10035–10046.

33 Y. Wu, J. Ward-Bond, D. Li, S. Zhang, J. Shi and Z. Jiang, g-C_3N_4@alpha-Fe_2O_3/C Photocatalysts: Synergistically Intensified Charge Generation and Charge Transfer for NADH Regeneration, *ACS Catal.*, 2018, **8**(7), 5664–5674.

34 M. Ahmad, X. Quan, S. Chen and H. T. Yu, Tuning Lewis acidity of MIL-88B-Fe with mix-valence coordinatively unsaturated iron centers on ultrathin Ti_3C_2 nanosheets for efficient photo Fenton reaction, *Appl. Catal., B*, 2020, **264**, 118534.

35 S. Zhong, Y. Xi, Q. Chen, J. Chen and S. Bai, Bridge engineering in photocatalysis and photoelectrocatalysis, *Nanoscale*, 2020, **12**(10), 5764–5791.

36 J. Wang, X. Zuo, W. Cai, J. Sun, X. Ge and H. Zhao, Facile fabrication of direct solid-state Z-scheme g-C_3N_4/Fe_2O_3 heterojunction: a cost-effective photocatalyst with high efficiency for the degradation of aqueous organic pollutants, *Dalton Trans.*, 2018, **47**(43), 15382–15390.

37 T. Guo, K. Wang, G. Zhang and X. Wu, A novel alpha-Fe_2O_3@g-C_3N_4 catalyst: Synthesis derived from Fe-based MOF and its superior photo-Fenton performance, *Appl. Surf. Sci.*, 2019, **469**, 331–339.

38 Y. Chen, H. Li, Q. Ma, J. Wang, Q. Che, G. Wang, Y. Li and P. Yang, Facile synthesis of various alpha-Fe_2O_3 micro/nanostructures: Highlighting on the enhanced catalysis activities by formation of bowl-like alpha-Fe_2O_3/Au composites, *Mater. Res. Bull.*, 2018, **103**, 285–293.

39 P. Huang, S. Xu, M. Zhang, W. Zhong, Z. Xiao and Y. Luo, Modulation doping of absorbent cotton derived carbon dots for quantum dot-sensitized solar cells, *Phys. Chem. Chem. Phys.*, 2019, **21**(47), 26133–26145.

40 S. Babar, N. Gayade, H. Shinde, P. Mahajan, K. H. Lee, N. Mane, A. Deshmukh, K. Garadkar and V. Bhuse, Evolution of Waste Iron Rust into Magnetically Separable g-C_3N_4-Fe_2O_3 Photocatalyst: An Efficient and Economical Waste Management Approach, *ACS Appl. Nano Mater.*, 2018, **1**(9), 4682–4694.

41 Y. Shen, Q. Han, J. Hu, W. Gao, L. Wang, L. Yang, C. Gao, Q. Shen, C. Wu, X. Wang, X. Zhou, Y. Zhou and Z. Zou, Artificial Trees for Artificial Photosynthesis: Construction of Dendrite-Structured alpha-Fe_2O_3/g-C_3N_4 Z-Scheme System for Efficient CO_2 Reduction into Solar Fuels, *ACS Appl. Energy Mater.*, 2020, **3**(7), 6561–6572.